Volume 12 | Number 12 | 28 March 2016 | Pages 2979–3128

# Soft Matter

www.softmatter.org

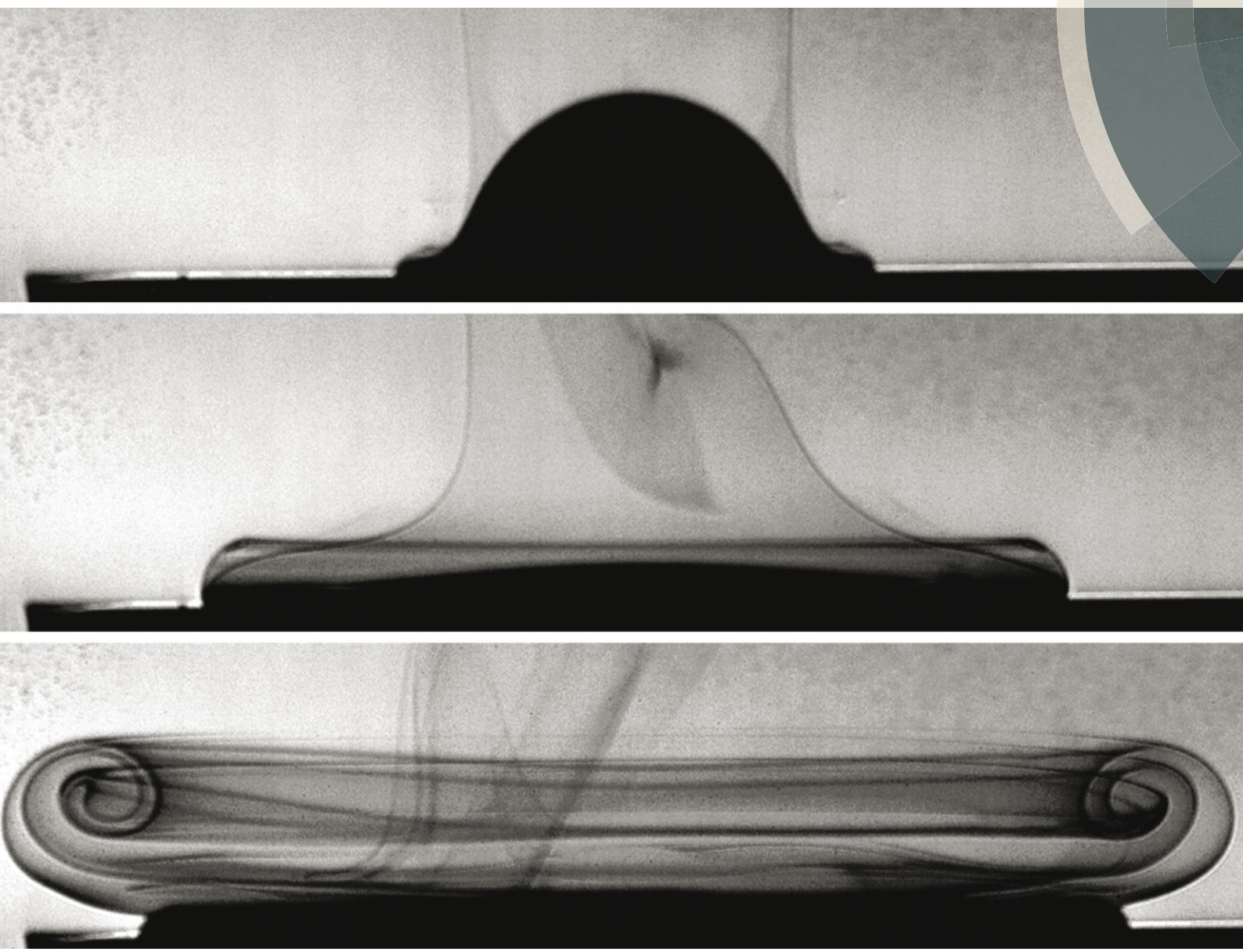

ISSN 1744-683X

ROYAL SOCIETY OF CHEMISTRY

PAPER
Irmgard Bischofberger *et al.*
Airflows generated by an impacting drop

175 YEARS

Soft Matter

PAPER

View Article Online
View Journal | View Issue

Cite this: *Soft Matter*, 2016, 12, 3013

# Airflows generated by an impacting drop†

Irmgard Bischofberger,*[a] Bahni Ray,[b] Jeffrey F. Morris,[cd] Taehun Lee[b] and Sidney R. Nagel[a]

Received 2nd November 2015,
Accepted 11th January 2016

DOI: 10.1039/c5sm02702k

www.rsc.org/softmatter



A drop impacting a solid surface with sufficient velocity will splash and emit many small droplets. However, lowering the ambient air pressure suppresses splashing completely. This effect, robustly found for different liquid and substrate properties, raises the fundamental question of how air affects a spreading drop. In a combined experimental and numerical study we characterize the flow of air induced by the drop after it hits the substrate, using a modified Schlieren optics technique combined with high-speed video imaging and Lattice-Boltzmann simulations. Our experiments reveal the emergence of air structures on different length scales. On large scales, the airflow induced in the drop's wake leads to vortex structures due to interaction with the substrate. On smaller scales, we visualize a ring structure above the outer edge of the spreading liquid generated by the spreading of the drop. Our simulations reveal the interaction between the wake vorticity and the flows originating from the rapidly escaping air from below the impacting drop. We show that the vorticity is governed by a balance between inertial and viscous forces in the air, and is unrelated to the splashing threshold.

## 1 Introduction

When a liquid drop hits a solid surface, it can break up into many droplets to produce a splash. A stunningly rich variety of splashes can be observed depending on the liquid properties[1–5] and the geometry and elasticity of the substrate.[6–10] Surprisingly, the splash of a liquid drop is suppressed when the ambient air pressure is lowered below a threshold value.[3,11–13] This remarkable sensitivity to gas pressure is found for a variety of distinct regimes of splashing; it applies to splashes of both low and high viscosity[3,14] and even for splashes on a rough surface where the overall form of the splash is significantly different.[8] The robustness of the effect suggests a common cause for the splash suppression;[15] the mechanism underlying how the surrounding gas affects splashing, however, is still unknown.[16–18] One suggestion to explain the air effect, associating the splash with a continuous air film below the drop, has been ruled out in extensive studies over the past few years.[5,16,19–22] While there is indeed air trapped below the center of the drop, there is no persistent air layer at the typical impact velocities relevant to splashing.

To develop insight into the effect of the air on the spreading liquid it is indispensable to understand the airflows that are generated by the impact and spreading of the drop.[21,23–25] Previous experiments investigating the collision of a solid sphere with a wall in a water tank revealed the generation of a complex vortex structure associated with the sphere impact.[26–28] In air, as the wake flow following the rigid sphere overtakes the sphere on impact, the resultant flows can cause significant air exchange near the surface. This vorticity generation is strong enough to levitate a layer of dust on the surface in the immediate neighborhood of the impact.[29]

In this paper, we show that the airflows generated by an impacting liquid drop have an even richer structure than those generated by a falling solid sphere. In addition to the vorticity generated by the momentum transfer of the moving drop falling through the air, which induces airflows on large length scales originating from the drop's wake, structures in the air are also created due to the rapid radial spreading of the liquid. The rapid escape of air from below the drop at impact further contributes to the dynamics of the vorticity. Our visualizations of these airflows (from both experiment and simulation) allow us to track the temporal evolution of the vortex trajectories for a wide range of impact, liquid and gas parameters. We show that the vortex dynamics is set by the relative importance of inertial to viscous forces in the air. These are distinct from the parameters that govern the splashing threshold.

[a] The James Franck and Enrico Fermi Institutes and The Department of Physics, The University of Chicago, Chicago, Illinois 60637, USA
[b] Department of Mechanical Engineering, City College of City University of New York, New York, 10031, USA
[c] Department of Chemical Engineering, City College of City University of New York, New York, 10031, USA
[d] Benjamin Levich Institute, City College of City University of New York, New York, NY 10031, USA. E-mail: irmgard.bischofberger@gmail.com

† Electronic supplementary information (ESI) available: Movies of the airflows generated by liquid drops impacting both smooth and rough dry substrates. See DOI: 10.1039/c5sm02702k

## 2 Methods

The drops used in this study are either mixtures of water and glycerol (Fisher Scientific), mixtures of water and ethanol (Fisher Scientific) or silicone oils (polydimethylsiloxane, Clearco Products) with kinematic viscosity $\nu_{\mathrm{liq}}$ ranging from 2.4 to 1012 mm$^2$ s$^{-1}$, as measured with glass capillary viscometers (Cannon-Fenske). Drops with radius $r$ ranging from 1.0 to 2.2 mm are created using a syringe pump and released from a height $h$ above a dry, glass substrate. This height sets the impact velocity $u_0 = \sqrt{2gh}$ which is varied between 1.4 and 4.2 m s$^{-1}$. We compare the airflows created by impacting drops with those induced from bouncing steel spheres of radius $r$ = 1.55 mm.

To study the effect of the ambient pressure on the airflows, we drop the liquids inside an acrylic tube that can be evacuated to varying pressures $P$ between 20 and 101 kPa. Within this pressure range the kinematic viscosity of the air $\nu_{\mathrm{air}}$ varies between 16 and 79 mm$^2$ s$^{-1}$ respectively. These parameters determine the Reynolds number of the air, $\mathrm{Re}_{\mathrm{air}} = 2ru_0/\nu_{\mathrm{air}}$, describing the ratio of inertial to viscous forces. Our experiments probe the range $94 < \mathrm{Re}_{\mathrm{air}} < 1180$.

We use Schlieren optics[30] as a tool to visualize changes in the refractive index of the surrounding air. We apply several methods to enhance the contrast in our images which are sensitive to different contributions of the airflows, as shown in Fig. 1. In our standard experiment, we heat a layer of glycerol, which is placed on the side of the substrate away from the impact area, to create a gradient of refractive index above the spreading liquid (Fig. 1, left panel). This method allows us to visualize the airflows generated from the fall of the drop, as well as those created at the moment of impact below the drop and those generated by the spreading liquid after impact. To decouple these various contributions, we perform a series of experiments where the drop either just barely misses the substrate or only partially hits the substrate, and continues to fall vertically. In these experiments, the flows in the drop's wake are unchanged but those associated with the drop impact and spreading are strongly reduced or entirely eliminated.

As this method relies on the gradient of index of refraction created by evaporating glycerol as a contrast agent, it could be thought to preferentially reflect the flows originating from the drop's wake where the gradient between pure air and glycerol vapor is strongest. To test for the robustness of the observed structures in the air we use a different contrast agent, a thin layer of 1,1,1,2-tetrafluoroethane (Miller-Stephenson), located directly above the substrate, which is not sensitive to the flows in the drop's wake (Fig. 1, right panel). We get good agreement between the two methods of visualization indicating that our standard method is sensitive to airflows from both the drop's wake and the air below the impact area.

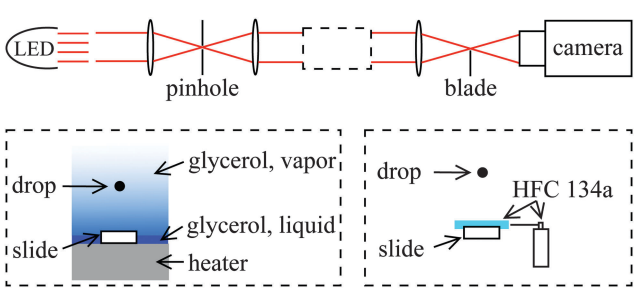


Fig. 1 Upper panel: schematics of the Schlieren imaging set-up used in the experiments. The dotted box denotes the test area. Lower panel: detailed description of the test area. Left: a thin liquid layer of glycerol evaporates on a heater. The glycerol vapor creates a gradient in index of refraction above the heater. Right: a thin layer of 1,1,1,2-tetrafluoroethane (HFC 134a) close to the area of impact of the drop is used as contrast agent.

We record the visible airflows at frame rates up to 20,000 fps using high-speed video imaging (Phantom v12, Vision Research).

In our simulations we use a lattice Boltzmann method (LBM), where we follow the evolution of a density probability distribution function for fictitious particles moving on a lattice. We employ the two-phase incompressible LBM,[31] which recovers the advective Cahn–Hilliard equation $\partial_t C + \nabla\cdot(\mathbf{u}C) = \nabla\cdot(M\nabla\mu)$, with the composition $C$, the adjustable mobility parameter $M$ and the chemical potential $\mu$, and the Navier–Stokes equations $\nabla\cdot\mathbf{u} = 0$ and $\partial_t(\rho\mathbf{u}) + \nabla\cdot(\rho\mathbf{u}\mathbf{u}) = -\nabla p - \rho\nabla\mu + \nabla\cdot\eta(\nabla\mathbf{u} + (\nabla\mathbf{u})^T)$, with the density $\rho$, the dynamic pressure $p$, and the molecular viscosity $\eta$. The superscript $T$ denotes the transpose of $\nabla\mathbf{u}$. The composition and the density are related by a linear relation given as $\rho = \rho_l C + \rho_a(1 - C)$, where $\rho_l$ and $\rho_a$ are the bulk densities of liquid and air, respectively. The chemical potential is obtained from the derivative of the free energy with respect to the order parameter. The free energy is given by

$$\Psi = \int_V \left[E_0(C) + \frac{\kappa}{2}|\nabla C|^2\right] \mathrm{d}V + \int_S \left[\phi_0 - \phi_1 C_s + \phi_2 C_s^2 - \phi_3 C_s^3 + \ldots\right] \mathrm{d}S, \quad (1)$$

where $V$ is the system volume and $S$ is the surface area of the substrate. The free energy of the system involves a mixing energy density for binary fluids, where $\kappa$ is the gradient parameter and $E_0(C) = \beta C^2(C - 1)^2$ is the bulk free energy with constant $\beta$; and surface terms which control the solid–liquid interactions with the surface concentration $C_s$. The profile of a planar interface is given by $C(z) = [1 + \tanh(2z/D)]/2$, where $z$ is the coordinate normal to the plane interface and $D$ is the interface thickness. Once the surface tension $\sigma$ and interface thickness $D$ are chosen, $\beta$ and $\kappa$ can be specified as $\beta = 12\sigma/D$ and $\kappa = \beta D^2/8$. Here the integral of the free energy on solid boundaries employs a cubic boundary condition, in which $\phi_0 = \phi_1 = 0$, $\phi_2 = \phi_c/2$, and $\phi_3 = \phi_c/3$ with $\phi_c$ being a constant to be chosen to recover the desired contact angle at equilibrium. The dimensionless wetting potential $\Omega_c = \phi_c\sqrt{2\kappa\beta}$, is related to the equilibrium contact angle by $\cos\theta_{\mathrm{eq}} = (\sigma_{\mathrm{sa}} - \sigma_{\mathrm{sl}})/\sigma_{\mathrm{la}} = -\Omega_c$, where $\sigma_{\mathrm{sa}}$, $\sigma_{\mathrm{sl}}$, and $\sigma_{\mathrm{la}}$ represent the surface tensions of solid/air, solid/liquid, and liquid/air, respectively. The contact angle is chosen to be 12°.

The swirling strength is calculated by a critical point analysis of the local velocity gradient tensor and its corresponding eigenvalues. The velocity gradient tensor has a pair of complex conjugate eigenvalues $(\lambda_{\mathrm{cr}} \pm i\lambda_{\mathrm{ci}})$.[32] The strength of the local

 

swirling motion is quantified by $\lambda_{ci}$, where $\lambda_{ci} = 0$ represents pure shear flow with an infinitely long ellipse shape and $\lambda_{ci} > 0$ represents more circular eddies or vortices.

In our simulations, the drops are released from heights ranging from 3–10$r$ with a specified initial velocity (the impact height is found to exhibit a negligible effect on the strength of the large scale vorticity). At impact, the drops have velocities corresponding to those used in the experiments.

## 3 Results and discussion

### Experimental observations

We investigate the airflows above a spreading drop generated by impact onto a dry glass substrate. Fig. 2 shows a time-series for the impact of a water–ethanol drop onto smooth glass for $Re_{air} = 612$. The drop splashes almost immediately after impact (a) and ejects many small droplets (b). As these droplets fly off, they leave trails in their wake (c) and (d) which are visualized with our Schlieren optics. On large scales, a vortex sheet is created which, at late times, curls up. However, the multitude of trails left by the small ejected droplets make it difficult to observe this structure clearly.

In order to observe cleanly the large-scale airflows produced only by the expansion of the liquid drop along the substrate surface, we suppress the ejection of the liquid droplets. This can be done by using a slightly roughened substrate which has been shown to suppress splashing.[8] Because substrate roughness only disturbs the region below the spreading liquid, the airflow above the drop is not significantly affected.

As an example of the airflows resulting from drop impact without ejected drops, Fig. 3 shows the impact at $Re_{air} = 685$ of a silicone oil drop of radius 1.4 mm onto a glass substrate with root-mean-square roughness $R_{rms} \approx 1$ μm. The falling drop induces flow in its wake prior to the impact, as shown in (a) and (b). Upon impact, the air below the drop is deflected upwards to form the air crown seen in (b) and (c). Simultaneously, the liquid spreads out radially and induces flow in the surrounding air, resulting in the generation of a ring structure above the outer edge of the spreading liquid. Fig. 3(c) shows that this ring initially remains bound to the leading drop edge. At late times, it detaches from the liquid. This is caused by the wake vortex that, continuing to move rapidly outwards, eventually overtakes the slower-moving liquid, leading to the detachment of the ring and to the formation of an elegant toroidal vortex sheet that expands and curls up into a roll, as shown in Fig. 3(d–f). These structures are also seen, albeit less clearly, in Fig. 2(b). Using higher viscosity liquids that do not eject droplets we have tested that the overall air structures obtained on rough and smooth substrates are identical, which justifies the use of rough substrates where the air visualization is cleaner.

The shape of the air crown observed right after impact exhibits a systematic dependence on the drop viscosity $\nu_{liq}$, as seen in the images in Fig. 4 which show snapshots of the crown for $\nu_{liq}$ ranging from 10 mm$^2$ s$^{-1}$ to 1012 mm$^2$ s$^{-1}$. With increasing $\nu_{liq}$, the curvature of the air crown changes from

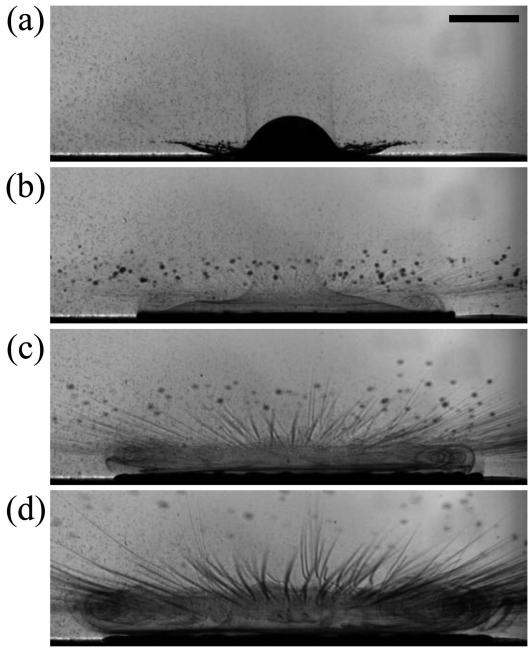


Fig. 2 The airflow created by the splash of a 1.25 mm radius water–ethanol drop ($\nu_{liq}$ = 2.4 mm$^2$ s$^{-1}$) at $Re_{air}$ = 612 hitting a smooth dry substrate photographed 0.25 ms (a), 1.75 ms (b), 3.25 ms (c) and 6.25 ms (d) after impact.[24] Vortical structures are generated in the air from the drop impact and the spreading of the liquid. In addition, the droplets ejected during the splash leave trails in their wake as they fly off. The scale bar is 2 mm.

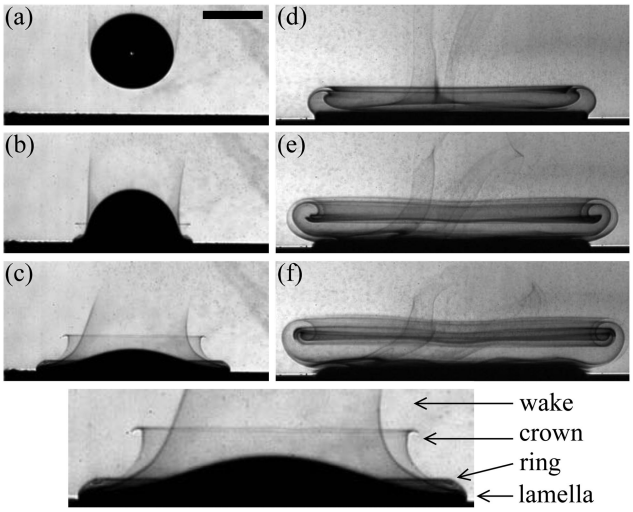


Fig. 3 Evolution of the airflow generated from the impact of a 1.4 mm radius drop of silicone oil ($\nu_{liq}$ = 20 mm$^2$ s$^{-1}$) at $Re_{air}$ = 685 on a rough dry substrate with root-mean-square roughness $R_{rms} \approx 1$ μm. The time after impact for each frame is: (a) −0.25 ms, (b) +0.25 ms, (c) 0.75 ms, (d) 1.75 ms, (e) 3.25 ms and (f) 4.25 ms.[24] (a) The falling drop generates a flow of air in its wake. (b and c) Immediately after impact, the air from the region below the drop is deflected into a crown. Spreading of the liquid induces the formation of a ring structure that is bound to the drop edge. (d–f) At later times, the airflow in the drop's wake convects outwards and curls into a toroidal structure, further inducing the detachment of the ring at the drop edge. The scale bar is 2 mm. Lowest panel: closeup indicating the wake, the crown, the ring at the edge of the lamella and the liquid lamella.

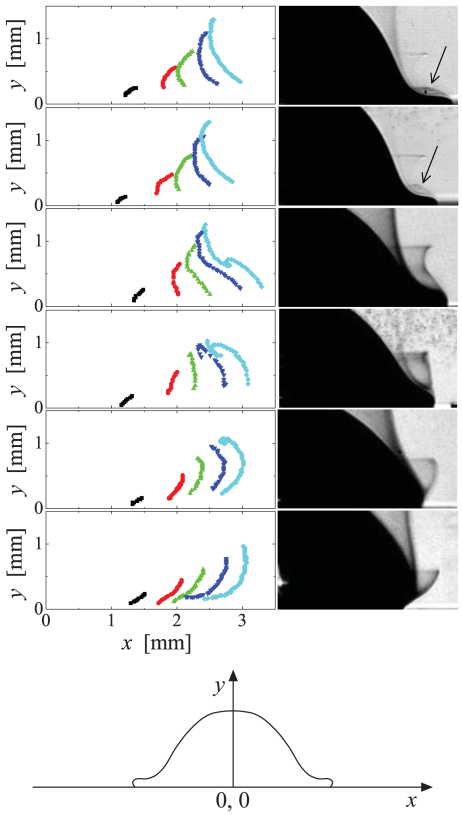


Fig. 4 Top: temporal evolution of the air crown at $Re_{air}$ = 587 for drop viscosities (from top to bottom): $\nu_{liq}$ = 10 mm$^2$ s$^{-1}$, 20 mm$^2$ s$^{-1}$, 52 mm$^2$ s$^{-1}$, 106 mm$^2$ s$^{-1}$, 356 mm$^2$ s$^{-1}$, 1012 mm$^2$ s$^{-1}$. The data sets correspond to times relative to impact of $t$ = 0.1 ms (black symbols), 0.3 ms (red symbols), 0.5 ms (green symbols), 0.8 ms (blue symbols) and 1.1 ms (cyan symbols). The origin ($x$ = $y$ = 0) is defined by the impact position of the drop. The images are snapshots of the crown shape at $t$ = 0.5 ms. The arrows in the first two images denote the ring structure above the edge of the liquid lamella. Bottom: schematics defining the origin, the $x$-axis and the $y$-axis.

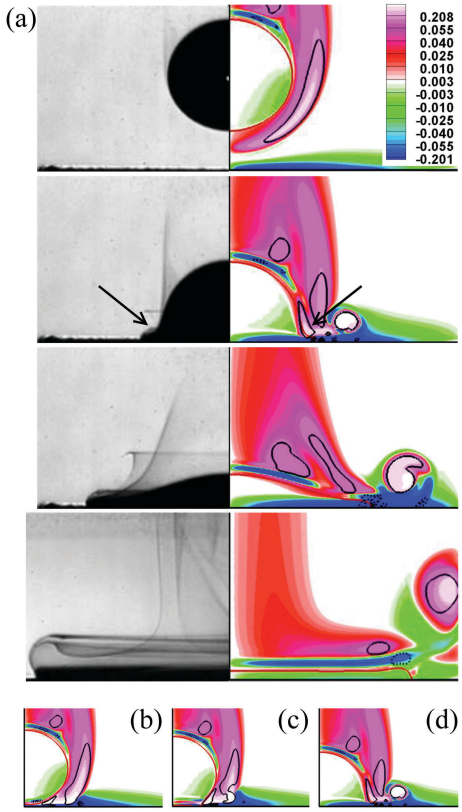


Fig. 5 (a) Comparison between the experimental visualizations (left) and the vorticity (flooded contour) and swirling strength isolines (black line contour) from the simulations (right) for an impact at $Re_{air}$ = 685 ($\nu_{liq}$ = 20 mm$^2$ s$^{-1}$). The time relative to impact for each frame is, from top to bottom: −0.25 ms, +0.25 ms, 0.75 ms, 1.75 ms. The airflows are generated in the wake of the drop. The experimentally detected structures follow the dynamics of the wake flow, the vorticity seen in the simulations exhibits a faster evolution due to rapidly escaping air from under the drop. The arrows in the second panel denote the ring above the edge of the liquid lamella. Lower panel: snapshots at (b) 0 ms, (c) 0.07 ms and (d) 0.25 ms showing the breakup of the swirling strength isolines in the wake due to rapid horizontal flows above the substrate.

negative to positive. The sign of the curvature is determined shortly after impact and remains unchanged as the crown grows.

The air crown appears to originate from the air displaced from beneath the drop. This is confirmed by the robustness of the crown signal to different imaging methods, where we get identical results using either glycerol vapor (which creates a far-ranged gradient of index of refraction above the substrate, see Methods) or a layer of 1,1,1,2-tetrafluoroethane (located only directly above the substrate) as contrast agents.

In this series of images we further note that the small-scale ring structure above the spreading lamella (indicated by an arrow in Fig. 4) is absent for drops with viscosity $\nu_{liq} > 20$ mm$^2$ s$^{-1}$; the ring forms only above a certain spreading velocity, suggesting as its origin the rapid spreading of the liquid lamella.

## Simulations

Several aspects of the experimentally observed features in the airflow are recovered in our simulations, as shown in Fig. 5(a), where we show a time sequence of both experimental and numerical visualizations. Before impact, the flows in the wake have developed during the fall of the drop (first panel). Upon impact, we recover the small-scale ring structure above the lamella's edge (indicated by arrows in the second panel) and at late times the curl-up of the vortex sheet. We note, however, that the numerics show a faster evolution of the airflows than that observed in the experiments. This is most evident in the third panel, where the vorticity contours have spread far beyond the drop lamella while the structures observed in the experiment have evolved to a lesser extent and are located above the lamella. To understand the origin of this enhanced dynamics of the vorticity we show in the lower panel of Fig. 5 details of the temporal evolution at early times. Focusing on the swirling strength isolines indicated by the black line contour, a measure of the local rotational component in the flow, we observe at impact three locations with high swirling strength; in the wake of the drop, close to the point of impact and to the side in the drop's wake (b). Considering the swirling strength to the side in

 

the drop's wake, we note that the isoline deforms significantly after impact (c). This deformation is due to the shear flow at the substrate created by the rapidly escaping air from below the drop. Eventually, the isoline breaks up and starts to roll up, getting carried away by the shear flow (d).

We currently do not have an explanation for the differences observed between the experimental and numerical visualizations, which affect both the location and the dynamics of the vorticity. We note though that the numerics probe the vorticity, while the experimental signal reflects the airflows. The displaced air from below the drop seemingly affects these two contributions differently.

It is interesting to compare our results of liquid drops to the impact of a solid sphere investigated by Thompson *et al.*[27] In both cases, vorticity is generated in the wake of the object and opposite-sign vorticity due to boundary layer formation on top of the object (blue signal located directly above the drop in Fig. 5(a, first panel)). For the solid sphere, the opposite-sign vorticity evolves together with the wake vorticity; the two contributions pass the sphere at the same rate and eventually combine in the curling up at later times. For the liquid drop, however, the evolution of the wake vorticity is faster than that of the opposite-sign vorticity. This increased dynamics of the wake is due to the airflow from underneath the drop, which induces an additional horizontal velocity component. The contribution of the flows from below the object is larger for the liquid drop because of the deformation and spreading of the drop.

### Analysis of vortex sheet

We characterize the lateral extent of the vortex sheet by defining a vortex-sheet radius $R$ as the distance from the center of the dropped object of radius $r$ (either the liquid drop or the solid sphere) to the furthest extent of the sheet (marked by the edge of the dark region above the leading edge of the spreading liquid) and take $R$–$r$ as a characteristic scale of the sheet extension, as shown in the inset of Fig. 6(a). After drop impact at $t = 0$ ms, $R$–$r$ increases rapidly before reaching its final value. The faster increase of the sheet extension seen in the numerics again reflects the increased dynamics due to the airflows from below the drop discussed above.

To characterize the temporal evolution of the circulation of the vortex sheet, we consider the height $h_{\mathrm{vortex}}$ of the ring structure with respect to the height of the spreading lamella, as indicated in the inset of Fig. 6(b) by a red arrow. This evolution is characterized by two distinct regimes. At early times, the ring is traveling with the spreading lamella and remains bound to its edge. At later times, the ring detaches from the lamella and moves outwards and upwards; the oscillations in the signal correspond to the curling up of the vortex sheet. This curling up is shown in the spatial trajectory of the vortex sheet shown in Fig. 6(c), which we extract experimentally by tracking the position of the ring (indicated by a red circle on the images in the inset of Fig. 6(c)). A qualitatively similar trajectory is observed for the vortex ring center position evaluated numerically (blue line).

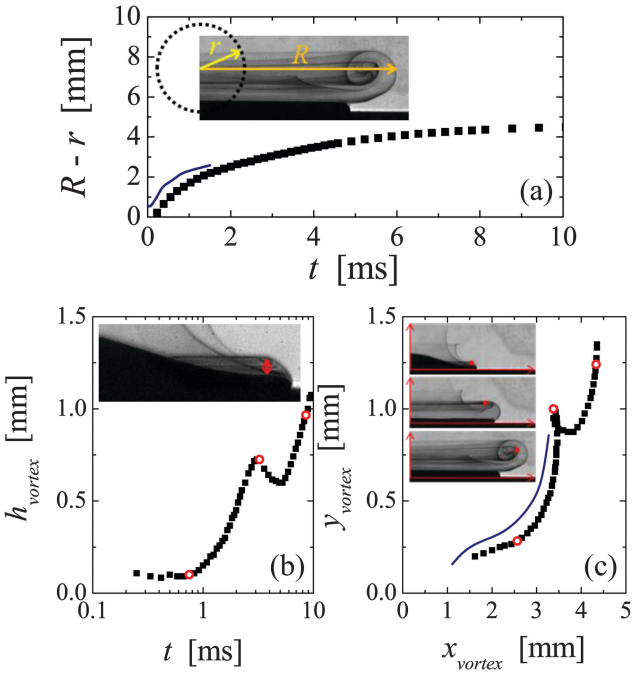


Fig. 6 Characteristics of the evolution of the airflows generated by an impacting and spreading drop at $\mathrm{Re}_{\mathrm{air}} = 513$. (a) Temporal evolution of the lateral extent of the vortex sheet $R$–$r$. The radius of the vortex sheet $R$ and the radius of the drop $r$ are defined in the image. The black symbols denote experimental results, the blue line numerical results. (b) Temporal evolution of the height $h_{\mathrm{vortex}}$ of the small-scale ring structure. $h_{\mathrm{vortex}}$ is measured from the top of the liquid lamella to the center of the ring, as indicated by the red arrow in the image. The ring initially remains bound to the drop but detaches at later times. The three red open circles correspond to the images shown in the inset to (c). (c) Tracking of the ring (indicated by red dots in the images) created by the spreading lamella allows reconstruction of the vortex trajectory in the experiments (black symbols). The maximum vorticity as calculated in the numerics exhibits a similar trend (blue line). The three red open circles correspond to the images. The origin ($x_{\mathrm{vortex}} = y_{\mathrm{vortex}} = 0$) is defined by the impact position of the drop.

The lateral extent of the vortex sheet is strongly dependent on the spreading of the drop after impact. This is seen in Fig. 7(a), where we show experimental and numerical images of impacts at a fixed $\mathrm{Re}_{\mathrm{air}} = 587$, for drops with varying viscosities (first four panels) and for a solid steel sphere (last panel). Clearly, the decrease in the radial spreading of the liquid with increasing viscosity of the drop leads to a systematic slowing of the expansion and a reduction of $R$–$r$, as shown in Fig. 7(b), where we report the temporal evolution of $r$ obtained from the experiments. We note that the strength of the vorticity decreases with increasing drop viscosity. We speculate that this dependence on $\nu_{\mathrm{liq}}$ is due to a change in the amount of air displaced from below the drop, which is set by the deformation of the drop upon impact.

While $R$–$r$ is dominated by the spreading of the liquid, the circulation characteristics of the vortex sheet, by contrast, exhibit similar behavior independent of the drop viscosity, as shown in Fig. 7(c). In particular, the detachment of the ring from the drop edge and the positions of the maxima and minima in the signal corresponding to the curling of the sheet

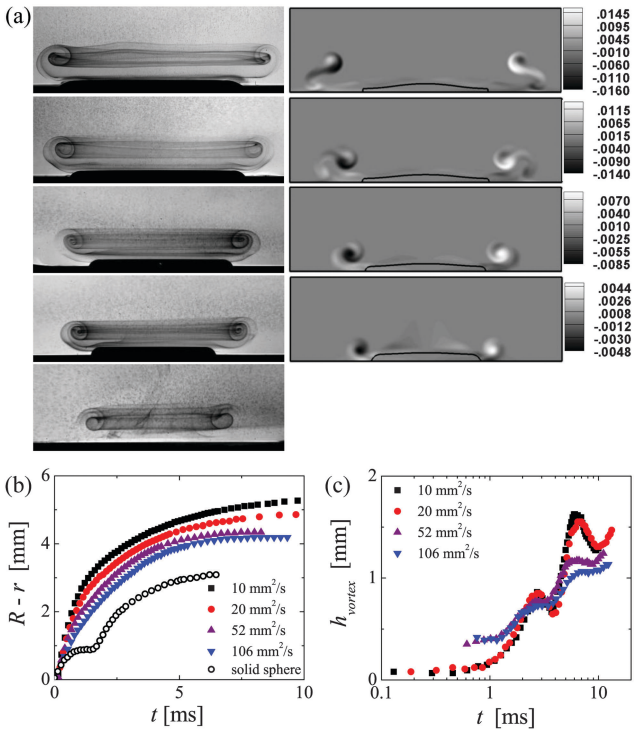


Fig. 7 Comparison between the airflows created by spreading drops of different viscosities $\nu_{liq}$ and those generated by a bouncing steel sphere at fixed $Re_{air}$ = 587 ($r$ = 1.55 mm, $u_0$ = 3.0 m s$^{-1}$). (a) Snapshots of the airflows from experiments at $t$ = 7 ms (left panel) and vorticity contours from numerics at $t$ = 1.75 ms (right panel). From top to bottom: drops with $\nu_{liq}$ = 10 mm$^2$ s$^{-1}$, $\nu_{liq}$ = 20 mm$^2$ s$^{-1}$, $\nu_{liq}$ = 52 mm$^2$ s$^{-1}$, $\nu_{liq}$ = 106 mm$^2$ s$^{-1}$ and solid sphere. (b) Temporal evolution of $R-r$, the radius of the vortex sheet, for the drops and sphere reported in (a, left panel). The lateral extent of the vortex sheet propagation decreases with increasing viscosity of the impactor and is much smaller for the solid sphere. (c) Temporal evolution of the height of the ring $h_{vortex}$ for the drops shown in (a, left panel). The rotational component characterized by the time sequence of the extrema of $h_{vortex}$ is independent of the drop viscosity, $\nu_{liq}$.

occur with similar dynamics. We here report $h_{vortex}$, the height of the ring with respect to the height of the spreading lamella as defined in Fig. 6(b) for the lower viscosity drops where a ring forms, while for the higher viscosity drops we consider a fold in the deflected air crown (as seen in the third panel in Fig. 4 at half the height of the crown) as our tracking feature. This results in the observed difference in the absolute values of $h_{vortex}$, but it is evident that the dynamics of the sheet circulation is independent of the drop viscosity.

### Parameters governing the airflows

To understand the parameters that govern the strength and dynamics of the sheet circulation, as well as the detachment of the ring structure, we first consider the effect of a change in the impact velocity, $u_0$, using drops of fixed viscosity and diameter. An increase in $u_0$ leads to a systematically earlier detachment of the ring, as shown in Fig. 8(a) which shows the temporal evolution of $h_{vortex}$ for experiments performed at three different $u_0$. We can rescale our data with the characteristic timescale ($2r/u_0$), which leads to a collapse of all data at early times, as

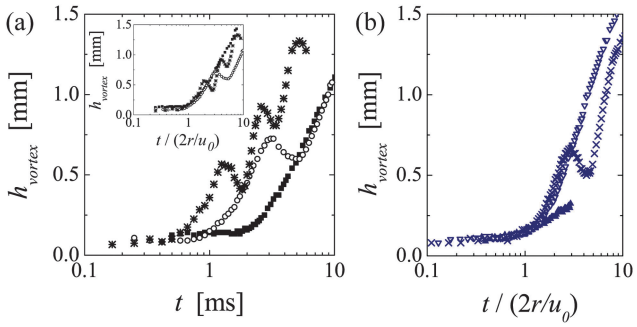


Fig. 8 (a) Temporal evolution of the height of the ring structure above the liquid lamella $h_{vortex}$ for a drop with radius $r$ = 1.4 mm impacting with velocity $u_0$ = 1.4 m s$^{-1}$ (filled squares), $u_0$ = 2.9 m s$^{-1}$ (open circles) and $u_0$ = 3.8 m s$^{-1}$ (stars) at atmospheric pressure $P$ = 101 kPa. Inset: normalization of the time with $2r/u_0$ leads to a master curve of the behavior at early times. The detachment of the ring occurs when the drop has spread by one drop diameter, $2r$. (b) Temporal evolution of the height of the ring structure above the liquid lamella $h_{vortex}$ for a drop with radius $r$ = 1.3 mm at pressure $P$ = 25 kPa (filled triangles), $P$ = 55 kPa (open triangles) and $P$ = 101 kPa (crosses) impacting with velocity $u_0$ = 2.9 m s$^{-1}$.

shown in the inset of Fig. 8(a). The detachment of the ring from the liquid edge occurs at $t/(2r/u_0) \approx 1$.

The late-time behavior also changes dramatically with a change in the impact velocity. The circulation of the vortex sheet becomes stronger with increasing $u_0$, inducing several rotations at the highest $u_0$. To test what other parameters set the strength of the vorticity, we further vary the pressure $P$ of the ambient gas which effectively changes the kinematic viscosity of the air, $\nu_{air}$, and the drop radius $r$. Examples of the airflows observed at different pressures are shown in Fig. 8(b). Remarkably, we find that the airflow is governed by one single parameter: the air Reynolds number $Re_{air} = 2ru_0/\nu_{air}$. As examples of the change in the circulation strength with $Re_{air}$ we show in Fig. 9(a) the trajectories of the vortex sheet for three representative experiments in the range $Re_{air}$ = 165 to $Re_{air}$ = 1179. While the vorticity is heavily damped at low $Re_{air}$, the circulation becomes increasingly stronger with increasing $Re_{air}$. We characterize the circulation by the total rotation angle $\theta$ the sheet experiences before it ceases to further curl up. The dependence of $\theta$ on $Re_{air}$ is shown in the upper panel of Fig. 9(b). We here include experiments where $Re_{air}$ is varied by either changing the ambient air pressure (open circles), or the impact velocity and the drop radius (solid squares). All data exhibit the same trend with $Re_{air}$, which implies that the vorticity is indeed entirely set by the balance between the inertial forces from the momentum transfer to the air during the fall of the drop and the viscous forces of the air which act as a damping term for the circulation. This is further confirmed in our numerical simulations, where we can evaluate the strength of the vorticity directly. Considering the maximum vorticity at $t$ = 1.75 ms, after the drop has ceased to spread, we again observe a qualitatively similar dependence of the maximum vorticity on $Re_{air}$, as shown in the lower panel of Fig. 9(b) where we report the vorticity normalized with that obtained at our highest $Re_{air}$ investigated.

 

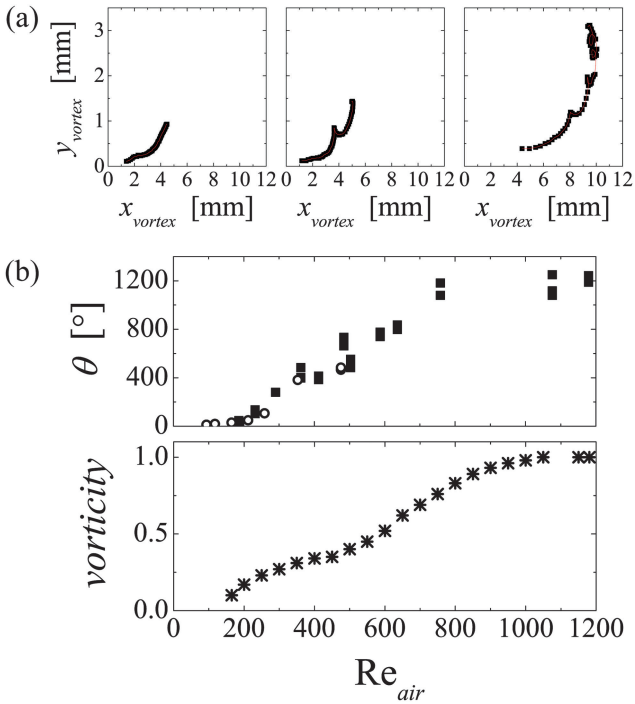


Fig. 9 (a) Experimental vortex sheet trajectories for $Re_{air}$ = 165 (first panel), $Re_{air}$ = 484 (second panel) and $Re_{air}$ = 1179 (third panel). The red lines are guides to the eye. (b) Upper panel: total rotation angle of the sheet, $\theta$, *versus* $Re_{air}$. Experiments performed by varying the ambient pressure $P$ are indicated by open circles, those performed by varying the drop radius $r$ and impact speed $u_0$ are indicated by filled squares. Lower panel: maximum vorticity obtained from the numerical simulations at $t$ = 1.75 ms as a function of $Re_{air}$. Both $\theta$ and the maximum vorticity exhibit a qualitatively similar dependence on $Re_{air}$; clearly, $Re_{air}$ is the sole parameter governing the late time evolution of the airflows.

## 4 Implications for splashing and conclusions

What does the dependence of the airflows on $Re_{air}$ tell us with regard to the role of air in splashing of drops? As mentioned in the introduction, while the crucial importance of the ambient air for the creation of a splash is undisputed, the mechanism by which air causes a drop to splash remains to be uncovered. A recent study by Stevens has experimentally determined splash criteria for low viscosity fluids on smooth substrates.[17] These criteria predict the transition from the splashing regime to the spreading regime to depend on three dimensionless numbers: $r/l_T$, the ratio of the drop radius to the gas mean free path $l_T$ (which accounts for the pressure dependence), the drop Reynolds number and the drop Weber number. This is a very involved dependence of the splash threshold on a large number of liquid, air and impact parameters. By contrast, our study shows that the airflows above the drop are governed by one single control parameter, the air Reynolds number $Re_{air}$. The air effect that determines the splash suppression at low pressure is thus seemingly unrelated to the vorticity generated by the impacting drop. Moreover, it is reasonable to assume that the effect of the vorticity on the spreading liquid is strongest within the time interval where the small-scale vortex ring remains bound to the drop edge, $t < (2r/u_0)$. The time interval during which a drop ejects a thin sheet that successively develops into a splash, however, is found to exceed significantly the criterion of $(2r/u_0)$, in particular for drops of higher viscosity or at reduced air pressure.[15,33] These considerations suggest that, rather than the airflows above the drop, the air in front of the leading edge of the spreading drop is responsible for destabilizing the liquid. This is consistent with recent studies that focused on the dynamics close to the contact line of the advancing liquid lamella,[9,34] although consensus has yet to emerge.[5]

Our experimental and numerical visualization reveal beautiful structures in the air induced by the interplay between impact and spreading of the liquid drop. We show that the rapid spreading of low-viscosity drops induces a ring structure above the edge of the liquid, which eventually detaches from the liquid edge due to interactions with the vorticity induced in the drop's wake. The elegant vortex structures that form at late times are due to inertial forces generating flows in the air that interact with the substrate. Viscous forces in the air damp out these structures, such that their evolution is determined by the competition between the two forces as characterized by the air Reynolds number $Re_{air}$.

## Acknowledgements

We thank Arnout Boelens, Roberto Cerbino, Andrzej Latka, Kelly W. Mauser and Tom Witten. This research was supported by the CCNY-University of Chicago MRSEC NSF PREM program DMR-0934206 and at UofC by the NSF MRSEC under DMR-0820054 and NSF Grant DMR-1105145. I. B. gratefully acknowledges financial support from the Swiss National Science Foundation (PBFRP2-134287). B. R. acknowledges financial support from a postdoctoral fellowship at City College of New York.

## References

1 M. Rein, *Fluid Dyn. Res.*, 1993, **12**, 61.
2 A. Yarin, *Annu. Rev. Fluid Mech.*, 2006, **38**, 159–192.
3 L. Xu, *Phys. Rev. E: Stat., Nonlinear, Soft Matter Phys.*, 2007, **75**, 056316.
4 C. Mundo, M. Sommerfeld and C. Tropea, *Int. J. Multiphase Flow*, 1995, **21**, 151–173.
5 C. Josserand and S. Thoroddsen, *Annu. Rev. Fluid Mech.*, 2016, **48**, 365–391.
6 J. C. Bird, S. S. Tsai and H. A. Stone, *New J. Phys.*, 2009, **11**, 063017.
7 R. E. Pepper, L. Courbin and H. A. Stone, *Phys. Fluids*, 2008, **20**, 082103.
8 A. Latka, A. Strandburg-Peshkin, M. M. Driscoll, C. S. Stevens and S. R. Nagel, *Phys. Rev. Lett.*, 2012, **109**, 054501.
9 Y. Liu, P. Tan and L. Xu, *Proc. Natl. Acad. Sci. U. S. A.*, 2015, **112**, 3280–3284.
10 C. Josserand, L. Lemoyne, R. Troeger and S. Zaleski, *J. Fluid Mech.*, 2005, **524**, 47–56.

11 L. Xu, W. W. Zhang and S. R. Nagel, *Phys. Rev. Lett.*, 2005, **94**, 184505.
12 J. Liu, H. Vu, S. S. Yoon, R. A. Jepsen and G. Aguilar, *Atomization Sprays*, 2010, **20**, 297–310.
13 N. K. Mishra, Y. Zhang and A. Ratner, *Exp. Fluids*, 2011, **51**, 483–491.
14 M. M. Driscoll, C. S. Stevens and S. R. Nagel, *Phys. Rev. E: Stat., Nonlinear, Soft Matter Phys.*, 2010, **82**, 036302.
15 C. S. Stevens, A. Latka and S. R. Nagel, *Phys. Rev. E: Stat., Nonlinear, Soft Matter Phys.*, 2014, **89**, 063006.
16 M. M. Driscoll and S. R. Nagel, *Phys. Rev. Lett.*, 2011, **107**, 154502.
17 C. S. Stevens, *Europhys. Lett.*, 2014, **106**, 24001.
18 S. Mandre and M. P. Brenner, *J. Fluid Mech.*, 2012, **690**, 148–172.
19 S. Mandre, M. Mani and M. P. Brenner, *Phys. Rev. Lett.*, 2009, **102**, 134502.
20 J. de Ruiter, D. van den Ende and F. Mugele, *Phys. Fluids*, 2015, **27**, 012105.
21 J. M. Kolinski, S. M. Rubinstein, S. Mandre, M. P. Brenner, D. A. Weitz and L. Mahadevan, *Phys. Rev. Lett.*, 2012, **108**, 074503.
22 L. Duchemin and C. Josserand, *Phys. Fluids*, 2011, **23**, 091701.
23 P. Tsai, R. CA van der Veen, M. van de Raa and D. Lohse, *Langmuir*, 2010, **26**, 16090–16095.
24 I. Bischofberger, K. W. Mauser and S. R. Nagel, *Phys. Fluids*, 2013, **25**, 091110.
25 C. Antonini, I. Bernagozzi, S. Jung, D. Poulikakos and M. Marengo, *Phys. Rev. Lett.*, 2013, **111**, 014501.
26 T. Leweke, M. C. Thompson and K. Hourigan, *Phys. Fluids*, 2004, **16**, L74–L77.
27 M. C. Thompson, T. Leweke and K. Hourigan, *J. Fluid Mech.*, 2007, **575**, 121–148.
28 J. R. Pacheco, A. Ruiz-Angulo, R. Zenit and R. Verzicco, *Phys. Fluids*, 2011, **23**, 063301.
29 I. Eames and S. Dalziel, *J. Fluid Mech.*, 2000, **403**, 305–328.
30 E. Hecht, *Optics*, Pearson Education Limited, 2001.
31 T. Lee and L. Liu, *J. Comput. Phys.*, 2010, **229**, 8045–8063.
32 R. Adrian, K. Christensen and Z.-C. Liu, *Exp. Fluids*, 2000, **29**, 275–290.
33 A. Latka, private communication.
34 G. Riboux and J. M. Gordillo, *Phys. Rev. Lett.*, 2014, **113**, 024507.

 